Supporting Information for "Numerical dynamo simulations reproduce palaeomagnetic field behaviour"

D. G. Meduri[1], A. J. Biggin[1], C. J. Davies[2], R. K. Bono[1], C. J. Sprain[3],

J. Wicht[4]

[1]Department of Earth, Ocean and Ecological Sciences, University of Liverpool, Liverpool, UK

[2]School of Earth and Environment, University of Leeds, Leeds, UK

[3]Department of Geological Sciences, University of Florida, Gainesville, FL, USA

[4]Department Planets and Comets, Max Planck Institute for Solar System Research, Göttingen, Germany

Contents of this file

1. Section S1: Governing equations

2. Figures S1 to S3

3. Tables S1 to S5

Additional Supporting Information (Files uploaded separately)

1. Caption for large Tables S1 and S5

Corresponding author: D. G. Meduri, Department of Earth, Ocean and Ecological Sciences, University of Liverpool, Liverpool, UK. (domenico.meduri@liverpool.ac.uk)

S1. Governing equations Here we provide further details on the numerical geodynamo models employed in this study. The dimensionless equations governing the system are: the momentum equation

$$\frac{\mathrm{Ek}}{\mathrm{Pm}}\left[\frac{\partial \mathbf{u}}{\partial t}+(\mathbf{u}\cdot\nabla)\,\mathbf{u}\right]=-\nabla p-2\hat{\mathbf{e}}_z\times\mathbf{u}+\frac{\mathrm{Pm}\,\mathrm{Ra}}{\mathrm{Pr}}C\frac{r}{r_\mathrm{o}}\hat{\mathbf{e}}_r+\mathrm{Ek}\nabla^2\mathbf{u}+(\nabla\times\mathbf{B})\times\mathbf{B}, \quad (1)$$

the induction equation

$$\frac{\partial \mathbf{B}}{\partial t}=\nabla\times(\mathbf{u}\times\mathbf{B})+\nabla^2\mathbf{B}, \quad (2)$$

the equation of evolution for the codensity

$$\frac{\partial C}{\partial t}+(\mathbf{u}\cdot\nabla)\,C=\frac{\mathrm{Pm}}{\mathrm{Pr}}\,\nabla^2 C+\gamma, \quad (3)$$

the continuity equation

$$\nabla\cdot\mathbf{u}=0 \quad (4)$$

and the solenoidal condition for the magnetic induction

$$\nabla\cdot\mathbf{B}=0. \quad (5)$$

Here $\mathbf{u}$, $\mathbf{B}$ and p are the (dimensionless) fluid velocity, magnetic induction and a modified pressure which includes centrifugal forces, respectively. The codensity C can stand for the super-adiabatic temperature fluctuations or the relative contribution of light elements in the outer core. The radial spherical coordinate is r and $\hat{\mathbf{e}}_r$ and $\hat{\mathbf{e}}_z$ denote the unit vectors in the radial direction and along the rotation axis, respectively. The above equations are obtained using the shell thickness d as length scale and the magnetic diffusion time $t_\eta = d^2/\eta$ as time scale. The magnetic induction $\mathbf{B}$ is scaled by $(\Omega\rho\mu_0\eta)^{1/2}$, where ρ is the reference fluid density and μ_0 the magnetic permeability of vacuum.

The dimensionless control parameters in the above equations are the Ekman number Ek, the Prandtl number Pr, the magnetic Prandtl number Pm (defined in Section 2.1) and the Rayleigh number Ra. Thermal dynamos are purely bottom heated, hence $\gamma = 0$ in Equation (3), and the Rayleigh number is defined as

$$\mathrm{Ra} = \frac{\alpha g_\mathrm{o} \beta d^2}{\Omega \kappa}, \tag{6}$$

where α is the fluid thermal expansivity, g_o is gravity at the outer boundary and β is the conductive temperature gradient at the outer boundary in the chemical dynamos. In chemical dynamos the Rayleigh number reads

$$\mathrm{Ra} = \frac{g_\mathrm{o} \Delta C \, d}{\Omega \kappa} \tag{7}$$

where ΔC is a codensity scale that depends on the inner codensity boundary condition employed (Wicht & Tilgner, 2010; Wicht & Meduri, 2016). The homogeneous sink term γ in Equation (3) serves to balance the codensity flux from the inner boundary.

The thermal dynamos were run using the numerical implementation of Willis, Sreenivasan, and Gubbins (2007) (further details on the code can be found in Davies et al., 2011). Simulations modelling pure chemical convection were instead performed using the code MagIC (Wicht, 2002; Schaeffer, 2013, available at `https://magic-sph.github.io`).

References

Davies, C. J., Gubbins, D., & Jimack, P. K. (2011). Scalability of pseudospectral methods for geodynamo simulations. *Concurrency and Computation: Practice and Experience*, *23*(1), 38-56. doi: 10.1002/cpe.1593

Schaeffer, N. (2013). Efficient spherical harmonic transforms aimed at pseudospectral

numerical simulations. *Geochemistry, Geophysics, Geosystems*, *14*(3), 751-758. doi: 10.1002/ggge.20071

Sprain, C. J., Biggin, A. J., Davies, C. J., Bono, R. K., & Meduri, D. G. (2019). An assessment of long duration geodynamo simulations using new paleomagnetic modeling criteria (qpm). *Earth and Planetary Science Letters*, *526*, 115758. doi: 10.1016/j.epsl.2019.115758

Wicht, J. (2002). Inner-core conductivity in numerical dynamo simulations. *Physics of the Earth and Planetary Interiors*, *132*(4), 281 - 302. doi: https://doi.org/10.1016/S0031-9201(02)00078-X

Wicht, J., & Meduri, D. G. (2016). A gaussian model for simulated geomagnetic field reversals. *Physics of the Earth and Planetary Interiors*, *259*, 45 - 60. doi: https://doi.org/10.1016/j.pepi.2016.07.007

Wicht, J., & Tilgner, A. (2010). Theory and modeling of planetary dynamos. *Space Science Reviews*, *152*(1), 501 - 542. doi: https://doi.org/10.1007/s11214-010-9638-y

Willis, A. P., Sreenivasan, B., & Gubbins, D. (2007). Thermal core-mantle interaction: Exploring regimes for "locked" dynamo action. *Physics of the Earth and Planetary Interiors*, *165*(1), 83 - 92. doi: https://doi.org/10.1016/j.pepi.2007.08.002

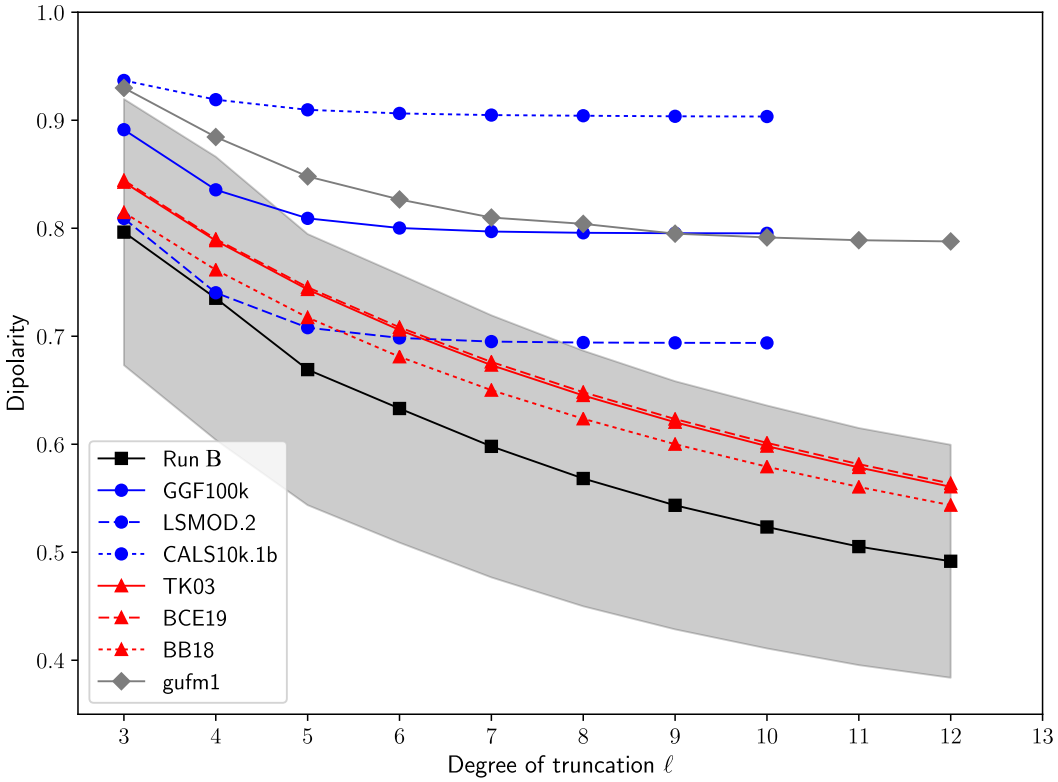

Figure S1. Dipolarity as function of its spherical harmonic degree of truncation ($\ell = 4$ and $\ell = 12$ correspond to D_4 and D_{12} respectively). Connected squares present run B, our most palaeomagnetic-like simulation (one standard deviation intervals above and below the dipolarity values are highlighted by the grey shaded region). Global palaeomagnetic field model reconstructions are shown by the connected blue circles and the statistical GGP models by the connected red triangles (see the legend inset). Connected diamonds show the historical field model gufm1. Note that the dipolarities of the palaeomagnetic field reconstructions saturate for degrees $\ell \geq 5$, since these models are well resolved up to $\ell = 4$.

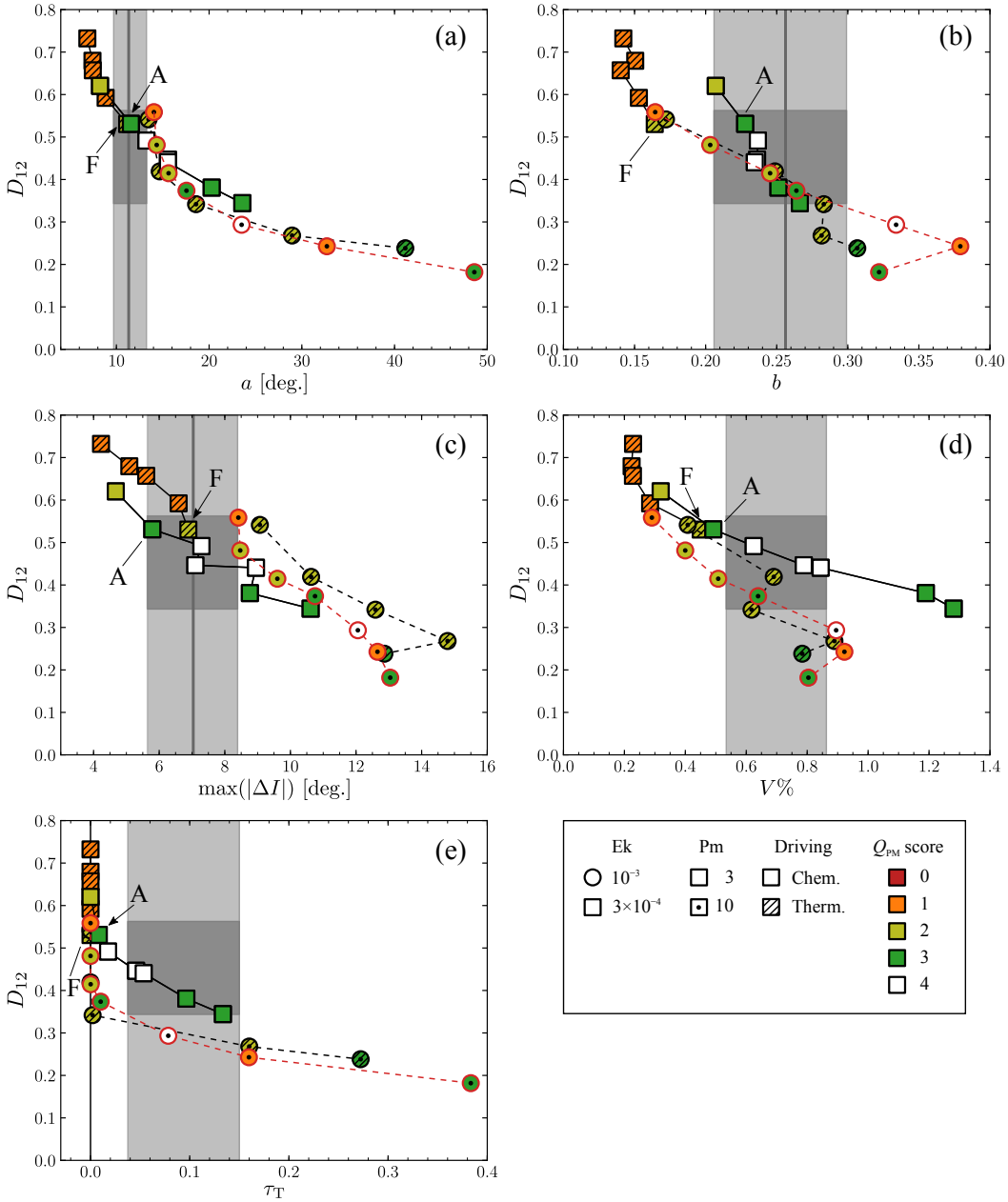

Figure S2. Same as Figure 2 but for two selected Rayleigh number tracks of the chemical and the thermal dynamos (the Rayleigh number increases for decreasing D_{12}). See the legend at the bottom right for the meaning of the symbols and Figure 1 for additional information on the selected tracks and on runs A and F.

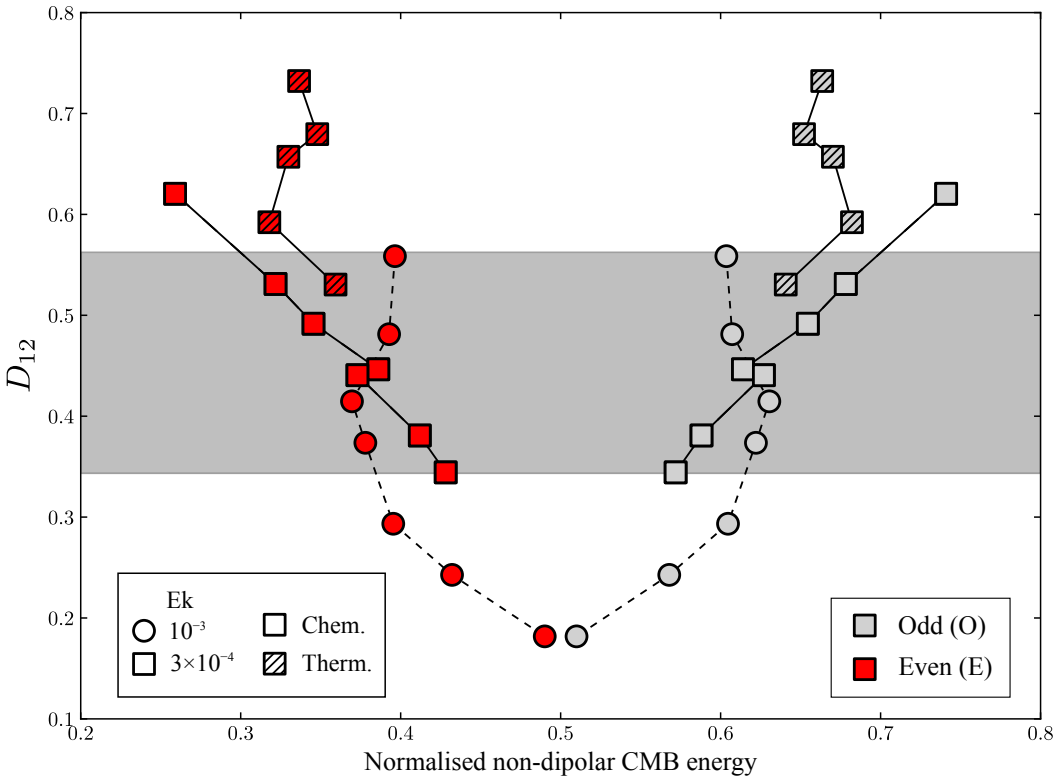

Figure S3. Dipolarity D_{12} as function of the normalised non-dipolar CMB energy for the odd (O) and even (E) spherical harmonic contributions. O (E) is a measure for the relative contribution of the equatorially antisymmetric (symmetric) field and is defined as the ratio of the time-averaged CMB Lowes power of the $\ell+m$ odd (even) harmonics for degrees $2 \leq \ell \leq 8$ to the time-averaged total power in these degrees. The three Rayleigh number tracks are the same of those shown in Figure 3.

Table S2. Regression coefficients of the quadratic fits (1) $Q^{\mathrm{m}}_{\mathrm{PM}} = c_0 + c_1 D_{12} + c_2 (D_{12})^2$ and (2) $Q^{\mathrm{m}}_{\mathrm{PM}} = c_0 + c_1 D_4 + c_2 (D_4)^2$ shown in Figure 1. The last column lists the coefficient of determination R^2.

Fit	Driving	c_0	c_1	c_2	R^2
(1)	Chem.	32.4	−128.6	142.0	0.85
	Therm.	32.0	−114.1	118.9	0.79
(2)	Chem.	65.2	−180.8	132.0	0.85
	Therm.	45.6	−120.3	89.5	0.84

Table S3. Dipolarity D_{12}, modified dipolarity D_4 and $Q_{\rm PM}$ metrics for the selected simulation runs A–F and the observational field models discussed in the main text. Standard deviations of D_{12} and D_4 are reported as errors. All measures are dimensionless except the equatorial dispersion a and the maximum absolute inclination anomaly $\max(|\Delta I|)$ which are given in degrees.

Model								Misfit					
	D_{12}	D_4	a	b	$\max(\lvert\Delta I\rvert)$	$V\%$	$\tau_{\rm T}$	a	b	ΔI	$V\%$	$\tau_{\rm T}$	Total
Run A	0.53 ± 0.09	0.77 ± 0.10	$11.56^{+0.80}_{-0.77}$	$0.23^{+0.03}_{-0.03}$	$5.8^{+3.2}_{-3.1}$	$0.49^{+0.03}_{-0.03}$	0.01	0.09	0.37	0.27	1.08	1.51	3.32
Run B	0.49 ± 0.11	0.74 ± 0.13	$13.24^{+1.06}_{-1.02}$	$0.24^{+0.04}_{-0.04}$	$7.3^{+4.0}_{-3.6}$	$0.62^{+0.03}_{-0.03}$	0.02	0.65	0.22	0.05	0.37	1.34	2.63
Run C	0.45 ± 0.13	0.69 ± 0.16	$15.57^{+1.46}_{-1.27}$	$0.24^{+0.05}_{-0.05}$	$7.1^{+4.6}_{-4.1}$	$0.79^{+0.04}_{-0.04}$	0.05	1.32	0.19	0.01	0.44	0.80	2.77
Run D	0.39 ± 0.14	0.65 ± 0.19	$16.92^{+1.89}_{-1.74}$	$0.24^{+0.08}_{-0.08}$	$7.3^{+5.3}_{-5.0}$	$0.91^{+0.05}_{-0.05}$	0.07	1.53	0.14	0.04	1.00	0.52	3.23
Run E	0.37 ± 0.07	0.62 ± 0.10	$17.56^{+1.13}_{-1.05}$	$0.26^{+0.04}_{-0.05}$	$10.8^{+4.5}_{-4.3}$	$0.64^{+0.03}_{-0.03}$	0.01	2.09	0.09	0.65	0.30	1.48	4.61
Run F	0.53 ± 0.06	0.80 ± 0.07	$11.16^{+0.63}_{-0.61}$	$0.16^{+0.02}_{-0.03}$	$6.9^{+1.2}_{-1.2}$	$0.45^{+0.02}_{-0.02}$	0.00	0.07	1.25	0.06	1.33	1.67	4.37
TK03	0.56 ± 0.14	0.79 ± 0.14	10.95	0.24	2.44	0.51	0.007	0.15	0.18	0.99	1.01	1.54	3.87
BCE19	0.56 ± 0.14	0.79 ± 0.14	10.14	0.25	2.22	0.50	0.004	0.46	0.10	1.05	1.03	1.59	4.23
BB18	0.54 ± 0.18	0.76 ± 0.18	12.70	0.27	2.16	0.71	0.035	0.38	0.12	0.90	0.29	1.05	2.74
GGF100k	-	0.84 ± 0.08	-	-	-	-	0.00	-	-	-	-	-	-
LSMOD2	-	0.74 ± 0.18	-	-	-	-	0.03	-	-	-	-	-	-
CALS10k.1b	-	0.92 ± 0.04	-	-	-	-	0.00	-	-	-	-	-	-
gufm1	0.79 ± 0.06	0.88 ± 0.03	-	-	-	-	0.00	-	-	-	-	-	-

Table S4. Q_{PM} observables estimated for Earth (from Sprain et al., 2019). All observables are dimensionless except the equatorial dispersion a and the maximum absolute inclination anomaly $\max(|\Delta I|)$ which are reported in degrees. The errors denote the estimated 95% confidence intervals or the assumed bounds.

a	b	$\max(\lvert\Delta I\rvert)$	$V\%$	τ_{T}
$11.33^{+1.93}_{-1.63}$	$0.26^{+0.04}_{-0.05}$	$7.04^{+1.35}_{-1.40}$	$0.70^{+0.17}_{-0.17}$	$0.094^{+0.056}_{-0.056}$

Table S1. Control parameters and time-averaged properties of the numerical geodynamo simulations explored in this study. Column 1 lists the model name; the prefix MAG (LED) refers to a simulation performed using the MagIC (Leeds) code (runs A–F are the cases discussed in the main text). 28 of these simulations were reported in previous studies (see the references listed in column 2: WM16 for Wicht and Meduri (2016) and S19 for Sprain et al. (2019); the model name assigned in these studies is given in parenthesis). The system control parameters, defined in Sections 2.1 and S1, are: the Ekman number Ek, the Rayleigh number Ra and the magnetic Prandtl number Pm. The Prandtl number Pr is 1 and the shell aspect ratio is $\chi = 0.35$ in all simulations. Column 6 details the convective driving mode (chemical or thermal). Column 7 lists the codensity boundary conditions (BCs): fixed codensity (C) or fixed codensity flux (F), with the first (second) letter referring to the inner (outer) boundary. $\epsilon = (q_{\max} - q_{\min})/\overline{q}$ is the amplitude of the lateral heat flux variations imposed at the outer boundary. Here $q_{\min}$, $q_{\max}$ and $\overline{q}$ are the minimum, maximum and average outer boundary heat flux, respectively. The heat flux pattern is a recumbent spherical harmonic of degree $\ell = 2$ and order $m = 0$. $\epsilon = 0$ refers to a homogeneous outer boundary. Column 9 lists the magnetic BCs: electrically insulating (I) or conducting (C), with the first (second) letter referring to the inner (outer) boundary. $t_{\rm sim}$ is the total simulation time (in units of the outer core magnetic diffusion time d^2/η). $\tau_{\rm T}$ and D_{12} are the relative transitional time and the dipolarity defined in the main article. The last column details the magnetic Reynolds number $\mathrm{Rm} = \mathrm{U}d/\eta$, where U is the time-averaged RMS core flow velocity. We note here that S19 report a wrong Rm for LEDA021 (Model 8).

Table S5. Additional summary simulation outputs used to construct Figures 1–3 in the main article. For definitions of the reported measures see the main text.